Supporting Information for Modeling of Diffusion of Acetone in UiO-66

Jacob J. Wardzala[1], Jonathan P. Ruffley[1], Isabella Goodenough[2], Allie M. Schmidt[1], Priyanka B. Shukla[1], Xin Wei[1], Abhishek Bagusetty[1,†], Mattheus De Souza[3], Prasenjit Das[3], Dorian J. Thompson[1,§], Christopher J. Karwacki[4], Christopher E. Wilmer[1,5], Eric Borguet[2], Nathaniel L. Rosi[1,3], J. Karl Johnson[1,]*

[1] Department of Chemical and Petroleum Engineering, University of Pittsburgh, Pittsburgh, Pennsylvania 15261, United States of America

[2] Department of Chemistry, Temple University, Philadelphia, Pennsylvania 19122, United States of America

[3] Department of Chemistry, University of Pittsburgh, Pittsburgh, Pennsylvania 15261, United States of America

[4] U.S. Army Combat Capabilities Development Command Chemical Biological Center, Aberdeen Proving Ground, Aberdeen, Maryland 21010, United States of America

[5]Department of Electrical and Computer Engineering, University of Pittsburgh, Pittsburgh, Pennsylvania 15261, United States of America

*Corresponding Author: J. Karl Johnson: karlj@pitt.edu

Present Addresses

†Argonne National Laboratory, 9700 S Cass Ave, Lemont, IL 60439

§Department of Chemical & Biomolecular Engineering, 191 Auditorium Road, #3222, Storrs Mansfield, CT, 06268

Table of Contents

Flexible UiO-66 force fields

Bonded potentials for the Boyd et al. UiO-66 potential[1] consist of bond stretching, angle bending, dihedral torsion, and improper torsion terms, as reported in the Supporting Information of Boyd et al. The Lennard-Jones parameters for the non-bonded interactions were taken from the UFF force field.[2] The atom-centered charges were computed from our DDEC6[3-6] calculations. As specified by Boyd et al., 1-4 non-bonded interactions were included. The Rogge et al. potential includes bond stretching, angle bending, dihedral torsion, and improper torsion terms as well as non-bonded interactions as reported by Rogge et al.[7] Non-bonded framework interactions use the MM3 van der Waals potential. Charge interactions are calculated using Gaussian charge densities. For interactions between framework atoms, 1-4 non-bonded Lennard-Jones interactions and 1-2, 1-3, and 1-4 non-bonded charge interactions were included. For cross interactions between the framework and adsorbate molecules, we used the same charges from our DDEC6 calculations, and Lennard-Jones terms from the UFF force field.[2] For the TraPPE/Rogge et al. potential, the Lennard-Jones terms for the UiO-66 μ_3-OH cross interactions with adsorbate molecules were modified to use parameters for oxygen and hydrogen from the TraPPE potential for isopropanol.[8] This was done because the TraPPE parameterization is designed to properly form hydrogen bonds.

Grand canonical Monte Carlo isotherms

Isotherms for N_2 and acetone were calculated using the RASPA[9] software package within the grand canonical ensemble using a setup that has been previously validated.[10-11] The isotherm of acetone at 298 K up to 100 kPa (saturation pressure is 30.6 kPa) is shown in Figure S1. Density-derived electrostatic and chemical (DDEC) charges for the atoms in each MOF were computed using the DDEC6[3-6] formalism. Ewald summation[12] was used to calculate electrostatic interactions. The Lennard-Jones parameters for the MOF atoms were taken from DREIDING[13]

except zirconium, which was taken from UFF.[2] The TraPPE[8] force field was used for acetone. The potential was truncated at a cutoff of 14.0 Å, and standard tail corrections were applied.[14] Lorentz−Berthelot combining rules were used for unlike interactions. A supercell containing eight formula units with fixed MOF atoms was used. Each pressure in the isotherm used at least 70,000 equilibration and 100,000 production cycles. One cycle was defined as N steps, where N was the number of adsorbates in the system at the beginning of each cycle. Additional simulations at very high pressures were also carried out to explore very high loading of acetone. Simulations at 1, 10, 100, and 1000 bar gave loadings of 5.90±0.1, 5.94±0.2, 6.1±0.4, and 7.4±0.1, respectively. We note that GCMC simulations used rigid UiO-66. At high pressures we expect that framework flexibility is important, so that the loading is likely underestimated. We also created models of defective UiO-66 with 8% (one missing linker per 2 formula units) and 4% (one missing linker per 4 formula units) missing linker defects. The charges were balanced by adding two formate groups for every missing linker removed. The formate groups also saturated all open metal sites on the SBU.

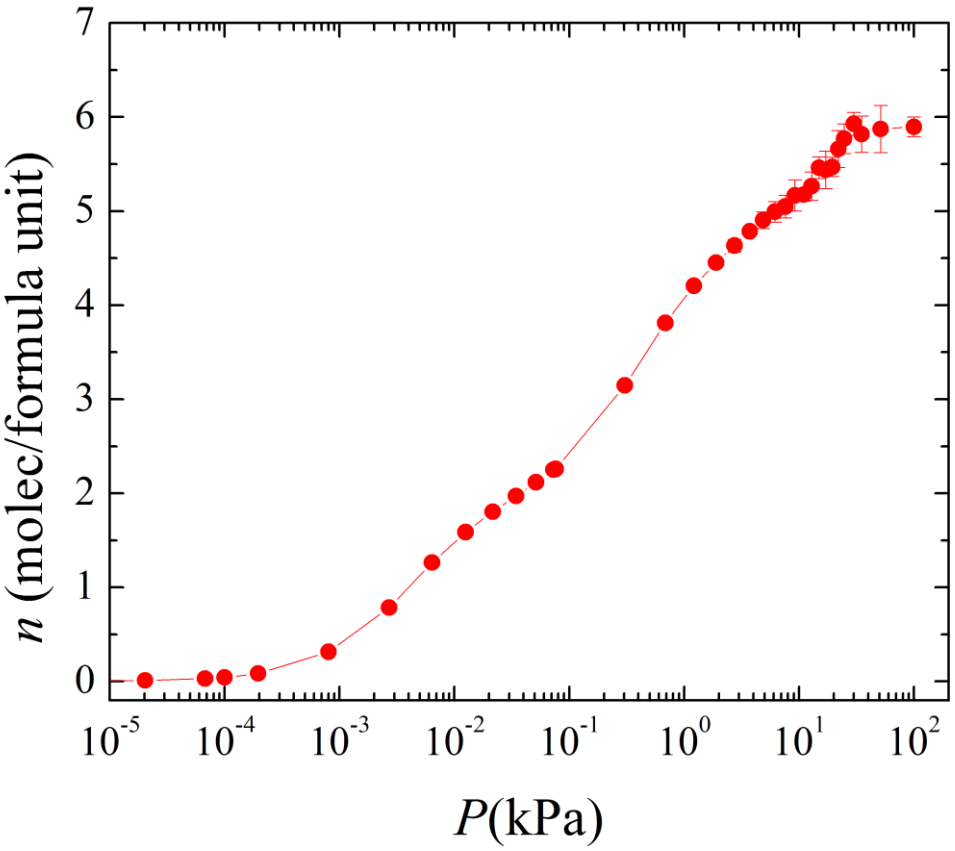

Figure S1. Simulated isotherm of acetone in pristine UiO-66 at 298 K computed from GCMC calculations.

CP2K simulation details

The ground state of an acetone molecule in UiO-66 was estimated via density functional theory (DFT) as implemented in CP2K 5.1[15-17] using our previously published procedure[18] for related work on dimethyl methylphosphonate in UiO-67 with some modifications. The Goedecker-Teter-Hutter pseudopotentials[19] were used with the DZVP-MOLOPT-SR basis set,[20] and Grimme's dispersion correction[21] was applied. The cutoff and relative cutoff were 400 Ry and 50 Ry, respectively. Convergence for these conditions has been verified previously[18] for UiO-67, which is expected to be transferable to UiO-66. The conjugate gradient orbital transformation minimizer[22] and LBFGS optimizer[23] were used. Relaxation calculations were performed on the UiO-66 primitive cell ($a = b = c = 14.83$ Å, $\alpha = \beta = \gamma = 60°$) and an acetone molecule padded with 15 Å of vacuum. A single acetone molecule was manually placed into the tetrahedral pore containing μ_3-OH groups of the UiO-66 primitive cell.

Ab initio molecular dynamics (AIMD) simulations in the canonical ensemble were carried out on the periodic system at a temperature of 1000 K using the GLE thermostat.[24-25] The AIMD simulations were run for 5 ps, using a timestep of 0.5 fs. The coordinates of the AIMD simulations were saved every 100 timesteps and the sampled geometries were relaxed to their local minima. The resulting energies were then used to calculate binding energies via Equation (S1).

$$\Delta E_{\text{bind}} = E_{AB} - E_A - E_B \quad \text{(S1)}$$

Synthesis materials and methods

All purchased chemicals were used without further purification except where otherwise noted: $ZrCl_4$ from Sigma-Aldrich, H_2-BDC, Conc. HCl, DMF, MeOH from Fisher Scientific. 4 Å molecular sieves, activated in an oven at 200°C for 2 days, were used to prepare dry solvents. Solvent was stored over the activated sieves for 1 day prior to use.

X-ray powder diffraction patterns were collected using a Bruker AXS D8 Discover powder diffractometer at 40 kV, 40 mA for Cu Kα, (λ = 1.5406 Å) from 3 to 40º at a step size of 0.02º. The data were analyzed using the EVA program from the Bruker Powder Analysis Software package. The simulated powder patterns were calculated using Mercury 3.10 from the CIF.

Thermogravimetric analyses (TGA) were performed using a TGA Q500 thermal analysis system under a N_2 atmosphere from room temperature to 800°C at a ramping rate of 1ºC/min. N_2 and acetone isotherms were collected using a Micromeritics 3Flex instrument.

UiO-66 Synthesis

The synthetic procedure for minimally defective UiO-66, shown in Scheme S1 is taken from Shearer et al.[26]

UiO-66 was synthesized by sequential addition of 378 mg of $ZrCl_4$ (1.62 mmol), 0.3 mL 35% HCl, and 9.75 mL of dry DMF into a clean 20 mL vial. The vial was capped and then sonicated for 10 minutes. To this mixture, 539 mg of H_2-BDC (3.24 mmol) was added, and the resulting mixture was further sonicated for an additional 20 minutes until the solution was completely transparent. The solution was then transferred to a 15 mL Teflon reactor, which was sealed within a stainless-steel autoclave and heated at 220°C for 21 h. After 21 h, the autoclave was removed from the oven and allowed to cool on the bench. After cooling, the product white microcrystalline powder was separated from solvent and washed with fresh dry DMF (10 mL, 3X).

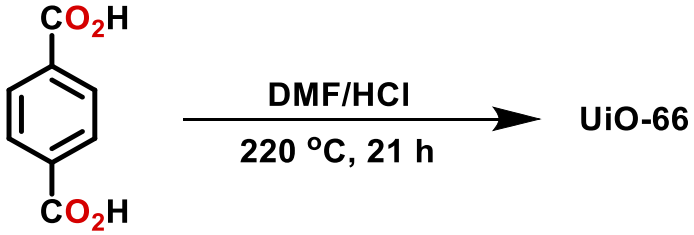

Scheme S1. Synthesis of UiO-66

UiO-66 Characterization

The product MOF was characterized using numerous analytical characterization methods to evaluate composition, structure, and defect levels.

PXRD. The bulk phase purity of UiO-66 was confirmed by PXRD which is in good agreement with the simulated pattern acquired from single-crystal diffraction data (Figure S2). No significant diffraction peaks were observed at low angles between 4-6.5° 2-theta, which is in agreement with the analysis of Shearer et al.[26] and expected for minimally defective UiO-66.

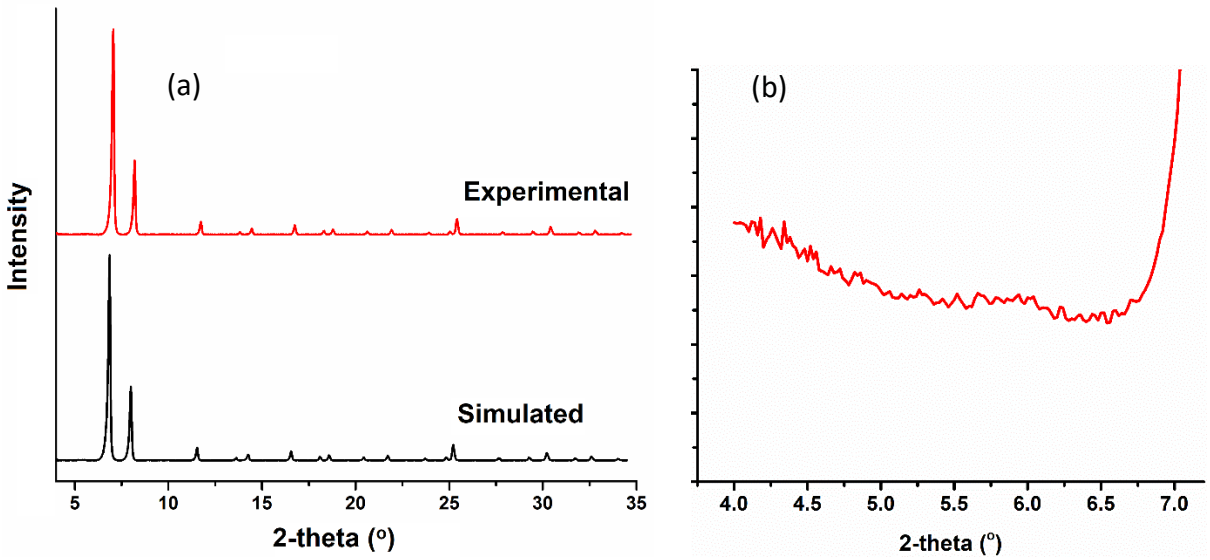

Figure S2. (a) Simulated (black) and Experimental (red) PXRD patterns of UiO-66. (b) No significant diffraction peak at low angles between 4 - 6.5 º 2-theta.

TGA. TGA was performed to determine the optimal activation condition and thermal stability of UiO-66 and also to quantify missing-ligand defects. The formula of defect-free UiO-66 MOF is $[(Zr_6O_6(BDC)_6).x(solvent)]$. The TGA profile of the synthesized material shows initial weight loss of lattice solvent water and DMF up to 250ºC followed by negligible weight loss up to 370ºC, indicating the compound was stable up to 370ºC. MOF decomposition was observed from 370-500ºC and results in formation of ZrO_2 (Figure S3). The decomposition weight loss is consistent with the expected combustion of a total of six BDC ligands, indicating minimally defective UiO-66. The calculations are detailed below.

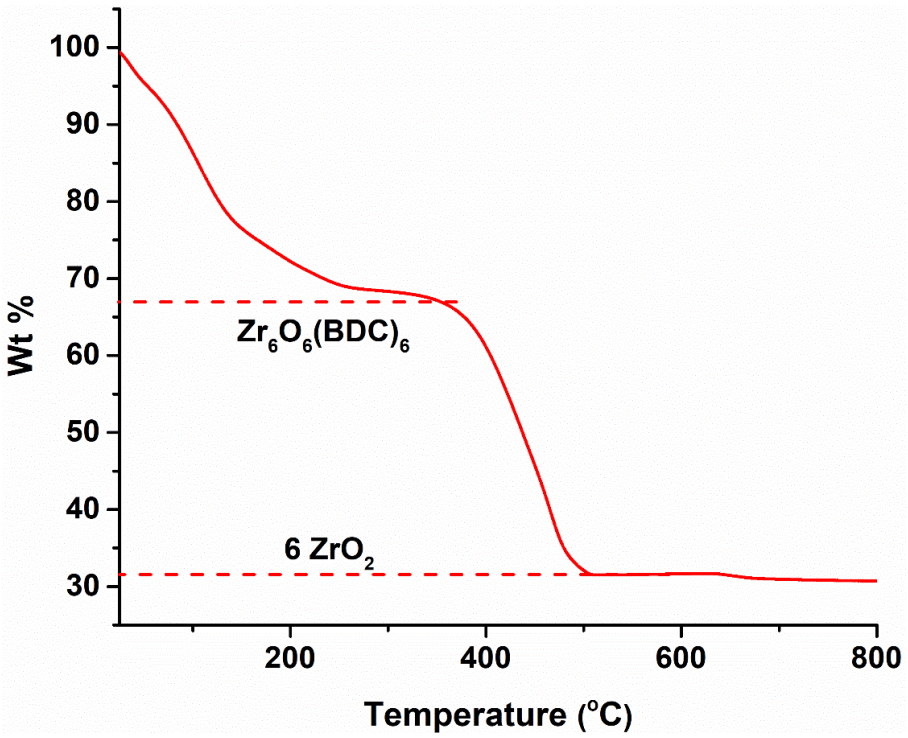

Figure S3. TGA profile of UiO-66. Dashed horizontal lines correspond to the formation $Zr_6O_6(BDC)_6$ (top) and 6 ZrO_2 (bottom).

Calculation of ligand defects

$$Zr_6O_6(BDC)_6 \xrightarrow{\Delta T} 6\ ZrO_2$$

$Zr_6O_6(BDC)_6$ MW: 1628.03 g/mol

ZrO_2 MW: 123.22 g/mol

10.475 g of sample (starting mass) was used for this analysis, and the end mass was 3.215 g. The end mass is the mass of ZrO_2 remaining after combustion. If UiO-66 is defect-free $Zr_6O_6(BDC)_6$, then after decomposition it will form 6 ZrO_2.

1. $3.215\ \text{mg}\ ZrO_2 \times \frac{1\ \text{mmol}\ ZrO_2}{123.22\ \text{mg}\ ZrO_2} = 0.02609\ \text{mmol}\ ZrO_2$
2. $0.02609\ \text{mmol}\ ZrO_2 \times \frac{1\ \text{mmol}\ Zr_6O_6(BDC)_6}{6\ \text{mmol}\ ZrO_2} = 0.004348\ \text{mmol}\ Zr_6O_6(BDC)_6$
3. $0.004348\ \text{mmol}\ Zr_6O_6(BDC)_6 \times \frac{1628.03\ \text{mg}\ Zr_6O_6(BDC)_6}{1\ \text{mmol}\ Zr_6O_6(BDC)_6} = 7.0792\ \text{mg}\ Zr_6O_6(BDC)_6$
4. $\frac{7.0792\ \text{mg}\ Zr_6O_6(BDC)_6}{10.475\ \text{mg}} \times 100\% = 67.57\%$ ← **Wt % of ideal MOF**

Gas and vapor adsorption studies

Sample Activation Procedure. After the as-synthesized sample was washed 3 times with dry DMF, the DMF molecules were exchanged with dry MeOH using the following specific procedure:

i) DMF was removed the solid sample via pipette;
ii) The solid was suspended in 15 mL dry MeOH and the resulting suspension was heated overnight at 90ºC;
iii) the sample was allowed to cool to room temperature, solvent was removed, and then the sample was washed with dry MeOH (3x);
iv) MeOH was removed and the sample was dried under a gentle Ar flow;
v) The dry powdered sample was then evacuated on a Micromeritics Smart VacPrep at 50ºC for 3 hours, 80ºC for 3 hours and 120ºC for 3 hours to yield activated sample. Fourier transform infrared spectroscopy was used to verify removal of solvent from the pores of activated UiO-66 samples (Figure S4).

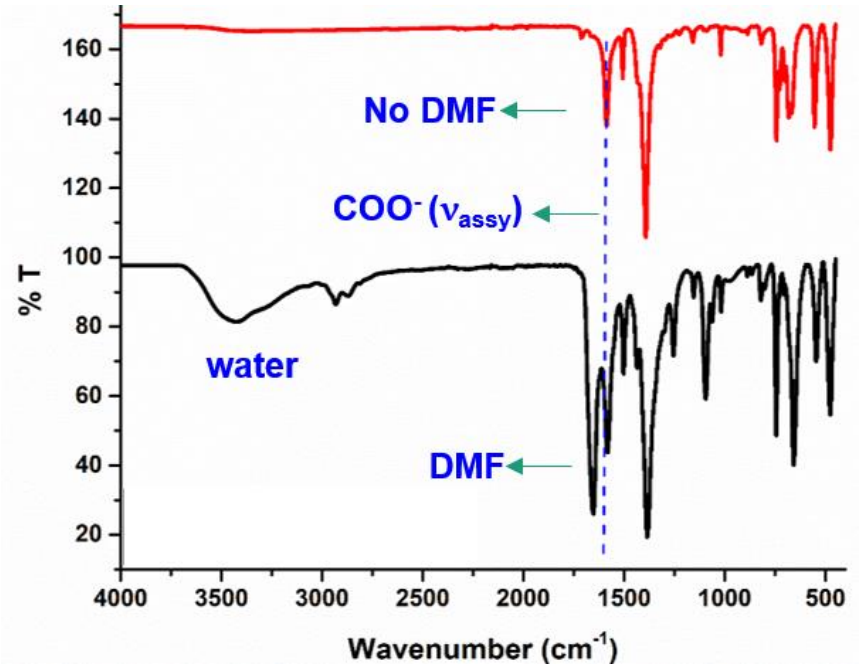

Figure S4. FTIR spectra of UiO-66 (black) and activated UiO-66 (red). Selected peaks (cm^{-1}): 3400 (b, lattice water), 1654 (s, DMF) and 1580 (s, COO^-). The carbonyl stretch for DMF was not observed in the activated sample.

N_2 Adsorption. The N_2 isotherms for MOF samples were collected at 77 K on a Micromeritics 3Flex instrument.

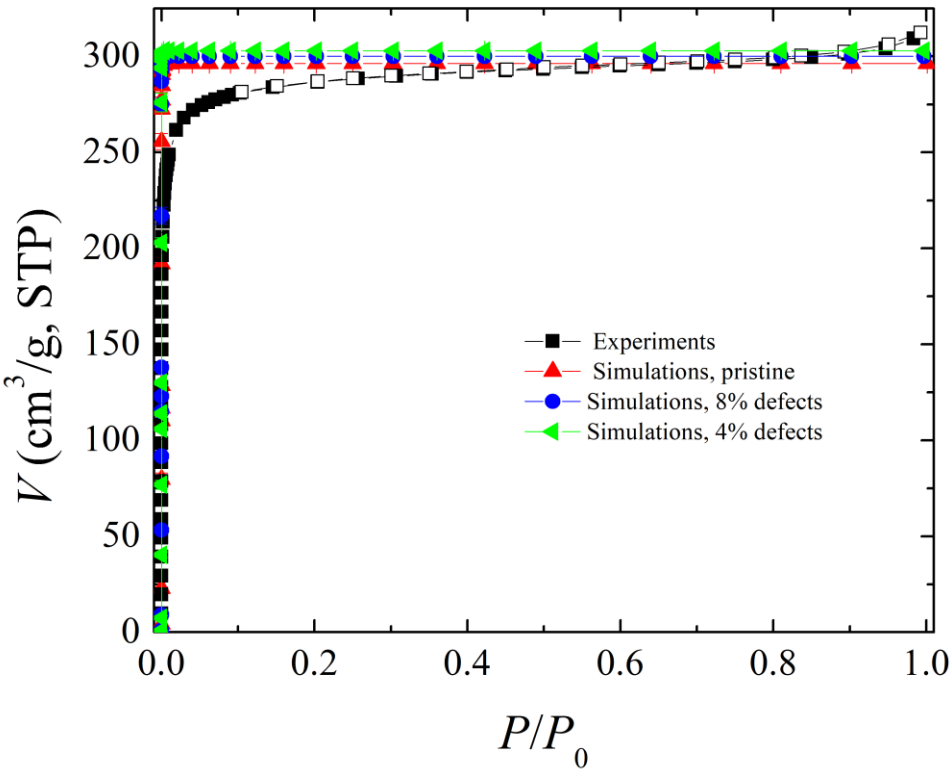

Figure S5. N_2 sorption isotherm of UiO-66 from experiments (squares) and simulations (up triangles for pristine, circles for 8%, and left triangles for 4% missing linker defects capped with formate groups). Closed and open squares represent adsorption and desorption, respectively.

The prepared UiO-66 sample shows a typical type I N_2 sorption isotherm from which a BET surface area of 1100 $m^2 g^{-1}$ was calculated (Figure S5). This surface is consistent with the report of Shearer et al.[26] for minimally defective UiO-66.

Acetone Adsorption. Acetone sorption was performed using activated UiO-66 sample. Adsorption isotherms were collected at 298K on a Micromeritics 3Flex instrument.

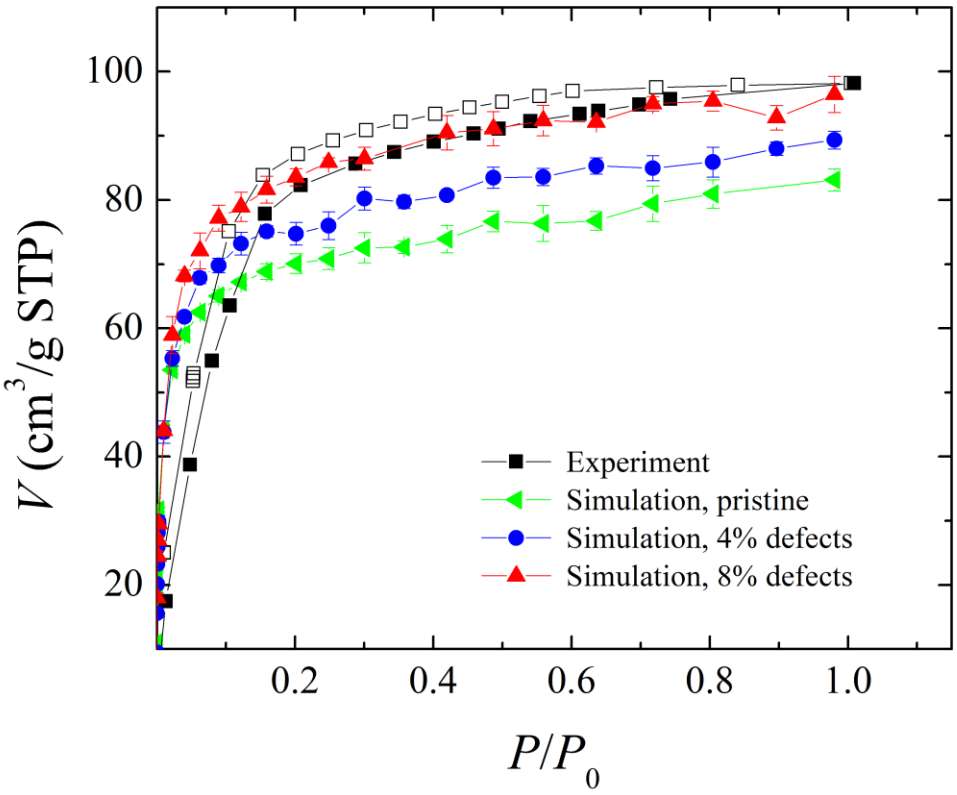

Figure S6. Acetone sorption isotherm of UiO-66 from experiments (squares) and simulations. Closed and open squares represent adsorption and desorption, respectively. The simulations are for pristine (green left triangles), 4% missing linkers with formate capping groups (blue circles), and 8% missing linkers (red up triangles).

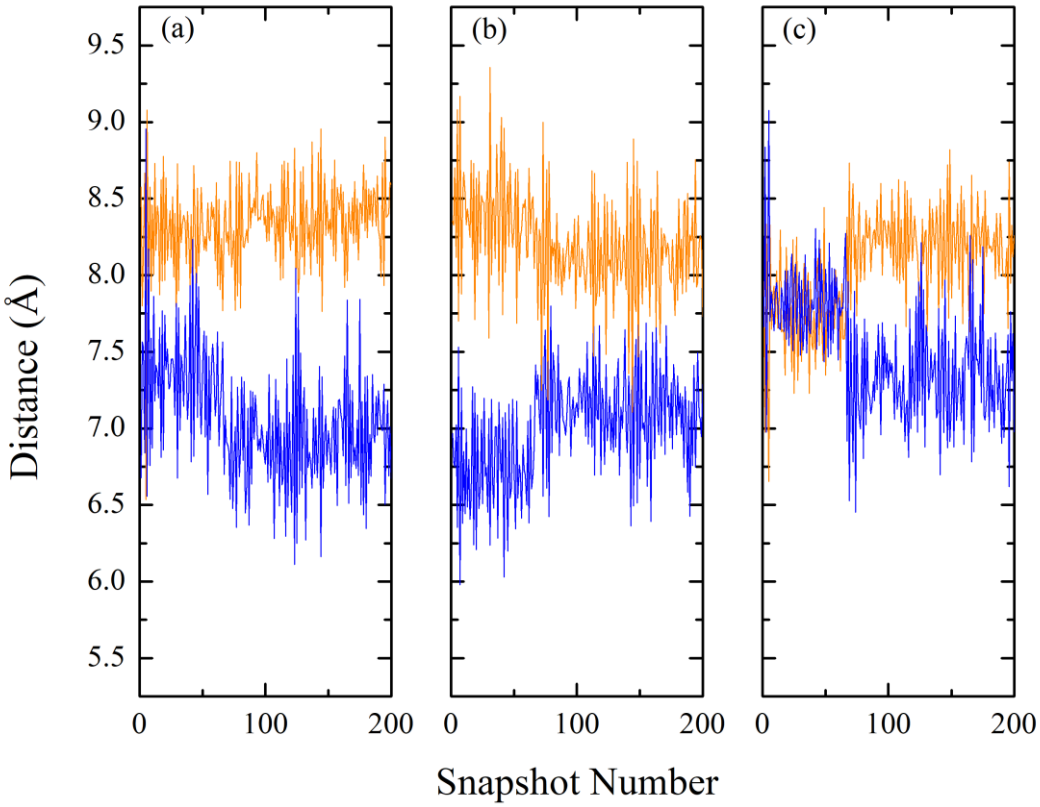

Figure S7. Distances between pairs of carbon atoms making up the window linkers as a function of time (snapshot) for empty UiO-66 at 325 K. The blue lines are for the side of the rings facing the octahedral and the orange lines are for the tetrahedral facing side of the rings. Distances shown between (a) linkers 1 and 2, (b) linkers 1 and 3, and (c) linkers 2 and 3, with linkers identified in Figure 4(d).

We have identified a problem with the Boyd et al. potential in representing the structure of the SBU. Upon relaxation the μ_3-O atoms of the SBU moved from their DFT-optimized positions to unphysical positions. Some of the μ_3-O atoms in each cluster moved toward the center of the SBU and overlapped with other μ_3-O atoms. This is shown in Figure S8. Only the atoms of the SBU are shown in that figure for clarity, although the relaxation was performed for the periodic (all atom) structure.

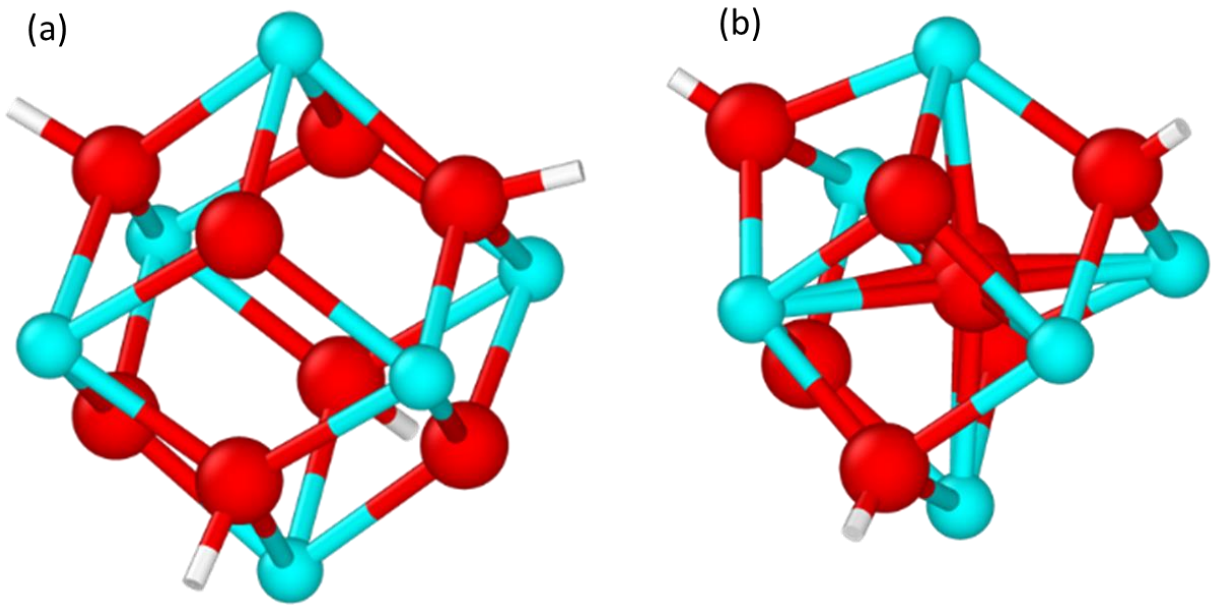

Figure S8. Change in the structure of the SBU going from the (a) initial structure to the (b) final relaxed structure using the Boyd et al. potential.[1] Only the atoms of the SBU are shown, although the relaxation was carried out for the full periodic structure. Oxygen is shown in red, zirconium in blue, and hydrogen in white.

Experimental Characterization Methods

Temperature-Programmed Desorption (TPD-MS) and Infrared (TP-IR) experiments were performed in a custom-built ultrahigh-vacuum (UHV) instrument described in detail previously.[27] MOF samples dispersed in dimethylformamide (DMF) were centrifuged at 14,000 rpm for five minutes, after which the wet MOF pellet (~2 mg) was extracted and uniformly pasted as a pinhole free disk (6 – 8 mm in diameter, 25 – 50 μm thick) directly onto a tungsten (W) grid (AlfaAesar, 25 μM thickness). The W-grid was then clamped to nickel supports and braced to a copper sample manipulator. A fast-response K-type thermocouple (Omega, 0.002" diameter) was welded to the grid adjacent to the MOF sample to monitor sample temperature. This design allows for rapid sample cooling to cryogenic temperatures (~100 K) and resistive heating using direct current from a power supply. After introduction into the UHV chamber, the resulting optical density measured by IR was on the order of 0.5 – 1.0. Custom LabVIEW programs (with commercial drivers) were used for all experiments to control the heating process in addition to monitoring temperature and pressure.

The UiO-66 sample activation process consists of UHV chamber baking at ~373 K for 18-24 hours followed by heating at 423 K for 15-30 mins. Baking the UHV chamber removed residual atmospheric gases (e.g., N_2, CO and water vapor) and laboratory contaminants adhered to the

chamber walls and sample manipulator. Heating the sample to 423 K allows for the removal of remaining weakly-physisorbed species within the UiO-66 pores.

Acetone purity was verified, after having undergone 5 consecutive free-pump-thaw cycles, using a shielded residual gas analyzer (AccuQuad RGA 300, Stanford Research Systems) installed in the UHV chamber. Acetone exposure was performed at 100 K by backfilling the UHV chamber at constant pressure (1.0×10^{-5} Torr) over a fixed time interval and monitored with a nude UHV ion gauge (Duniway iridium filament). 1000 L of acetone (note: 1 Langmuir (L) = exposure of 1.0×10^{-6} Torr for 1 s) was dosed onto a cold MOF surface (100 K), after which the pressure in the UHV chamber was allowed to recover below 5.0×10^{-8} Torr before sample heating was initiated. For TPD-MS experiments, select mass fragments (m/z = 15, 43 and 58 amu) were selectively monitored during sample heating at 2 K/s following acetone exposure.

Infrared spectra were collected in situ using an FTIR spectrometer (Tensor 27, Bruker) via OPUS 7.5 software. Spectra were recorded in transmission mode with a spectral range between 4000 cm^{-1} to 400 cm^{-1} as an average of 16 scans with 4 cm^{-1} using a room-temperature DLaTGA detector. Before each experiment, a 64-scan background spectrum was collected using the bare W-grid as a reference. To monitor analyte diffusion, the UiO-66 sample was heated linearly at 0.5 K/s from 100 K to 240 K and compared to the initial IR spectrum collected following acetone adsorption (1000 L) at 100 K.

Density functional theory results

The lowest energy configurations identified from DFT calculations of acetone in each of the three types of pores in UiO-66, namely the tetrahedral with μ_3-OH, tetrahedral with μ_3-O, and octahedral pores, are shown in Figures S9 through S11. Computed binding energies and differences in binding energies are given in Table S1.

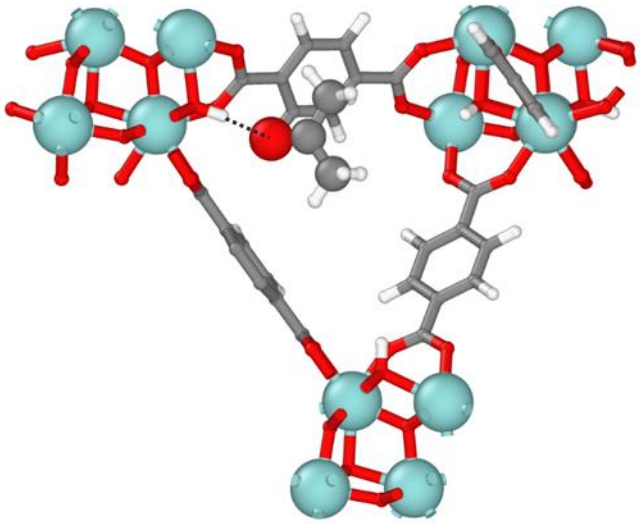

Figure S9. Configuration of local minima with the most favorable binding energy for acetone in UiO-66. The hydrogen bond between μ_3-OH and the ketone oxygen is shown by the black dashed line. Atoms are as follows: White: H, gray: C, red: O, cyan, Zr. Created with OVITO.[28]

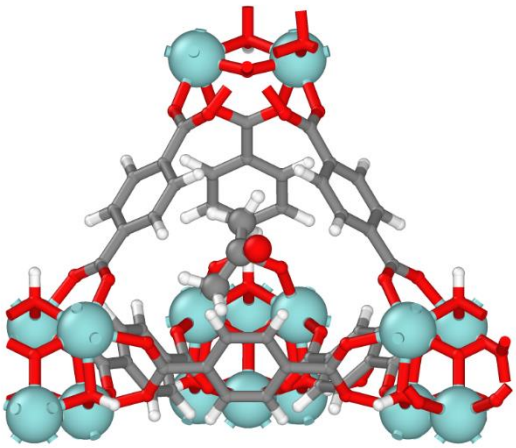

Figure S10. Configuration of local minima with the most favorable binding energy for acetone in the μ_3-O tetrahedral pore of UiO-66. Atoms are as follows: White: H, gray: C, red: O, cyan, Zr. Created with OVITO.[28]

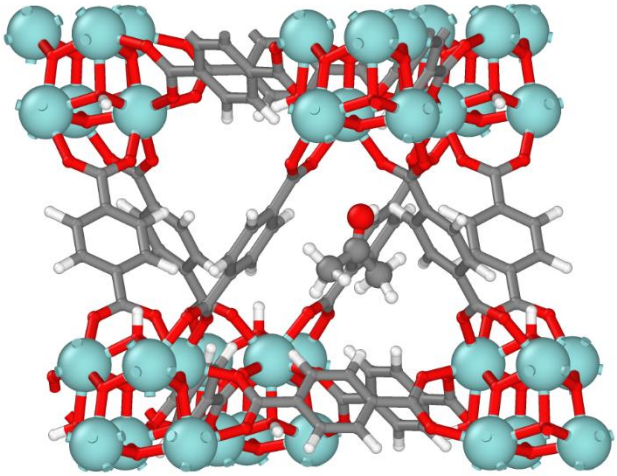

Figure S11. Configuration of local minima with the most favorable binding energy for acetone in the octahedral pore of UiO-66. Atoms are as follows: White: H, gray: C, red: O, cyan, Zr. Created with OVITO.[28]

Table S1. Binding energies and relative binding energies of acetone in the three types of pores computed from DFT.

Pore	ΔE_{bind} (kJ/mol)	$\Delta\Delta E_{bind}$ (kJ/mol)
Tetrahedral with μ_3-OH	-87.5	0
Tetrahedral with μ_3-O	-59.0	28.5
Octahedral	-48.8	38.7

TPD-MS results

Temperature-Programmed Desorption (TPD-MS) was used to identify the binding sites and energies for acetone adsorbed on the UiO-66 MOF. The similarity of the temperature profiles obtained for the most abundant molecular ion fragments for acetone (i.e., m/z = 15, 43 and 58 amu) indicates intact molecular desorption of acetone and suggests that the primary mode of interaction with UiO-66 is through physisorption.[29] Following a 1000 L acetone exposure, two distinct binding TPD peaks are observed at 148 K and 258 K (Figure S12). The low temperature feature (148 K) is associated with acetone sublimation from a multilayer, most likely condensed on the external surface of the MOF crystallites. The peak at 258 K is reflective of acetone physisorption within the MOF pore environment.

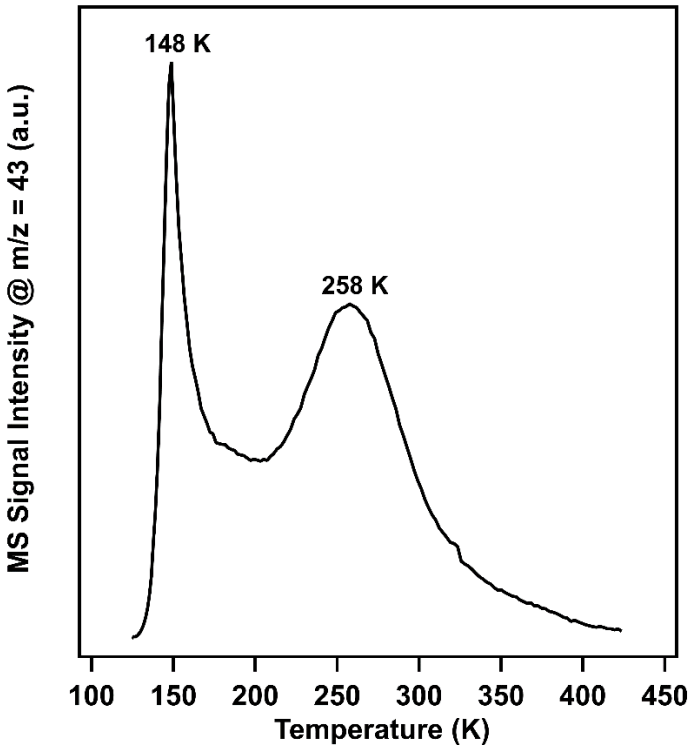

Figure S12. Thermal desorption profile for a 1000 L acetone exposure on UiO-66 revealing two desorption sites at 148 K (external multilayer) and 258 K (internal physisorbed).

We employ the Redhead analysis method,[30] described in detail in our previous work,[18] to calculate the acetone binding energy for the physisorbed site (258 K). It is important to note that the Redhead method assumes a first-order desorption process, typically with a pre-exponential factor of 10^{13} s^{-1}.[30] The true pre-exponential factor for this desorption process is unknown, and thus we provide a range of binding energies for a series of pre-exponential factors (Table S2).

Table S2. Calculated binding energies for various pre-exponential factors using Redhead analysis method.

Pre-exponential Factor (s^{-1})	**E_{des} (kJ/mol)**
10^{15}	76.8
10^{14}	71.9
10^{13}	67.0
10^{12}	62.0
10^{11}	57.1
10^{10}	52.1

Table S3. Binding energies and relative binding energies of acetone in the three types of pores computed using the Rogge et al. potential.

Pore	**ΔE_{bind} (kJ/mol)**	**$\Delta\Delta E_{bind}$ (kJ/mol)**
Tetrahedral with μ_3-OH	-58.0	0
Tetrahedral with μ_3-O	-52.5	5.5
Octahedral	-34.2	23.8

Table S4. Binding energies and relative binding energies of acetone in the three types of pores computed using the TraPPE/Rogge et al. potential.

Pore	**ΔE_{bind} (kJ/mol)**	**$\Delta\Delta E_{bind}$ (kJ/mol)**
Tetrahedral with μ_3-OH	-75.4	0
Tetrahedral with μ_3-O	-52.6	22.8
Octahedral	-34.5	40.9

References

1. Boyd, P. G.; Moosavi, S. M.; Witman, M.; Smit, B., Force-Field Prediction of Materials Properties in Metal-Organic Frameworks. *J. Phys. Chem. Lett.* **2017**, *8*, 357-363.
2. Rappe, A. K.; Casewit, C. J.; Colwell, K. S.; Goddard, W. A.; Skiff, W. M., UFF, a Full Periodic Table Force Field for Molecular Mechanics and Molecular Dynamics Simulations. *J. Am. Chem. Soc.* **1992**, *114*, 10024-10035.
3. Manz, T. A.; Limas, N. G., Introducing DDEC6 Atomic Population Analysis: Part 1. Charge Partitioning Theory and Methodology. *RSC Adv.* **2016**, *6*, 47771-47801.
4. Manz, T. A., Introducing DDEC6 Atomic Population Analysis: Part 3. Comprehensive Method to Compute Bond Orders. *RSC Adv.* **2017**, *7*, 45552-45581.
5. Limas, N. G.; Manz, T. A., Introducing DDEC6 Atomic Population Analysis: Part 4. Efficient Parallel Computation of Net Atomic Charges, Atomic Spin Moments, Bond Orders, and More. *RSC Adv.* **2018**, *8*, 2678-2707.
6. Limas, N. G.; Manz, T. A., Introducing DDEC6 Atomic Population Analysis: Part 2. Computed Results for a Wide Range of Periodic and Nonperiodic Materials. *RSC Adv.* **2016**, *6*, 45727-45747.
7. Rogge, S. M. J.; Wieme, J.; Vanduyfhuys, L.; Vandenbrande, S.; Maurin, G.; Verstraelen, T.; Waroquier, M.; Van Speybroeck, V., Thermodynamic Insight in the High-Pressure Behavior of UiO-66: Effect of Linker Defects and Linker Expansion. *Chem. Mater.* **2016**, *28*, 5721-5732.
8. Stubbs, J. M.; Potoff, J. J.; Siepmann, J. I., Transferable Potentials for Phase Equilibria. 6. United-Atom Description for Ethers, Glycols, Ketones, and Aldehydes. *J. Phys. Chem. B* **2004**, *108*, 17596-17605.
9. Dubbeldam, D.; Calero, S.; Ellis, D. E.; Snurr, R. Q., RASPA: Molecular Simulation Software for Adsorption and Diffusion in Flexible Nanoporous Materials. *Mol. Simul.* **2015**, *42*, 81-101.
10. Mohamed, M. H.; Yang, Y.; Li, L.; Zhang, S.; Ruffley, J. P.; Jarvi, A. G.; Saxena, S.; Veser, G.; Johnson, J. K.; Rosi, N. L., Designing Open Metal Sites in Metal–Organic Frameworks for Paraffin/Olefin Separations. *J. Am. Chem. Soc.* **2019**, *141*, 13003-13007.
11. Agrawal, M.; Sava Gallis, D. F.; Greathouse, J. A.; Sholl, D. S., How Useful Are Common Simulants of Chemical Warfare Agents at Predicting Adsorption Behavior? *J. Phys. Chem. C* **2018**, *122*, 26061-26069.
12. Ewald, P. P., Die Berechnung optischer und elektrostatischer Gitterpotentiale. *Annalen der Physik* **1921**, *369*, 253-287.
13. Mayo, S. L.; Olafson, B. D.; Goddard, W. A., DREIDING: a generic force field for molecular simulations. *J. Phys. Chem.* **1990**, *94*, 8897-8909.
14. Allen, M. P.; Tildesley, D. J., *Computer Simulations of Liquids*, Second edition. ed.; Oxford University Press: Oxford, United Kingdom, 2017, p xiv, 626 pages.
15. Frigo, M.; Johnson, S. G., The Design and Implementation of FFTW3. *Proc. IEEE* **2005**, *93*, 216-231.

16. VandeVondele, J.; Krack, M.; Mohamed, F.; Parrinello, M.; Chassaing, T.; Hutter, J., Quickstep: Fast and Accurate Density Functional Calculations Using a Mixed Gaussian and Plane Waves Approach. *Comput. Phys. Commun.* **2005**, *167*, 103-128.
17. VandeVondele, J.; Hutter, J., An Efficient Orbital Transformation Method for Electronic Structure Calculations. *J. Chem. Phys.* **2003**, *118*, 4365-4369.
18. Ruffley, J. P.; Goodenough, I.; Luo, T.-Y.; Richard, M.; Borguet, E.; Rosi, N. L.; Johnson, J. K., Design, Synthesis, and Characterization of Metal–Organic Frameworks for Enhanced Sorption of Chemical Warfare Agent Simulants. *J. Phys. Chem. C* **2019**, *123*, 19748-19758.
19. Goedecker, S.; Teter, M.; Hutter, J., Separable Dual-Space Gaussian Pseudopotentials. *Phys. Rev. B* **1996**, *54*, 1703-1710.
20. VandeVondele, J.; Hutter, J., Gaussian Basis Sets for Accurate Calculations on Molecular Systems in Gas and Condensed Phases. *J. Chem. Phys.* **2007**, *127*, 114105.
21. Grimme, S.; Antony, J.; Ehrlich, S.; Krieg, H., A Consistent and Accurate Ab Initio Parametrization of Density Functional Dispersion Correction (DFT-D) for the 94 Elements H-Pu. *J. Chem. Phys.* **2010**, *132*, 154104.
22. Weber, V.; VandeVondele, J.; Hutter, J.; Niklasson, A. M. N., Direct Energy Functional Minimization Under Orthogonality Constraints. *J. Chem. Phys.* **2008**, *128*.
23. Liu, D. C.; Nocedal, J., On the Limited Memory BFGS Method for Large Scale Optimization. *Math. Program.* **1989**, *45*, 503-528.
24. Ceriotti, M.; Bussi, G.; Parrinello, M., Langevin Equation with Colored Noise for Constant-Temperature Molecular Dynamics Simulations. *Phys. Rev. Lett.* **2009**, *102*, 020601.
25. Ceriotti, M.; Bussi, G.; Parrinello, M., Nuclear Quantum Effects in Solids Using a Colored-Noise Thermostat. *Phys. Rev. Lett.* **2009**, *103*, 030603.
26. Shearer, G. C.; Chavan, S.; Ethiraj, J.; Vitillo, J. G.; Svelle, S.; Olsbye, U.; Lamberti, C.; Bordiga, S.; Lillerud, K. P., Tuned to Perfection: Ironing Out the Defects in Metal–Organic Framework UiO-66. *Chem. Mater.* **2014**, *26*, 4068-4071.
27. Kwon, S.; Vidic, R.; Borguet, E., The Effect of Surface Chemical Functional Groups on the Adsorption and Desorption of a Polar Molecule, Acetone, from a Model Carbonaceous Surface, Graphite. *Surface Science* **2003**, *522*, 17-26.
28. Stukowski, A., Visualization and analysis of atomistic simulation data with OVITO–the Open Visualization Tool. *Modell. Simul. Mater. Sci. Eng.* **2010**, *18*.
29. Kwon, S.; Russell, J.; Zhao, X. C.; Vidic, R. D.; Johnson, J. K.; Borguet, E., Combined Experimental and Theoretical Investigation of Polar Organic Adsorption/Desorption from Model Carbonaceous Surfaces: Acetone on Graphite. *Langmuir* **2002**, *18*, 2595-2600.
30. Redhead, P. A., Thermal Desorption of Gases. Vacuum, 1962; Vol. 12, pp 203-211.